Materials Advances

PAPER

Check for updates

Enhancing the magnetic properties of superparamagnetic iron oxide nanoparticles using hydrothermal treatment for magnetic hyperthermia application

Carla Martins,[a] Catarina Rolo,[a] Vanessa R. G. Cacho,[b] Laura C. J. Pereira, [iD][b] João Paulo Borges, [iD][a] Jorge Carvalho Silva, [iD][c] Tânia Vieira[c] and Paula I. P. Soares [iD] *[a]

Superparamagnetic iron oxide nanoparticles (SPIONs) are the most commonly used inorganic nanoparticles for magnetic hyperthermia in cancer treatment. In this technique, the temperature of the tumor is increased by applying an external alternating magnetic field, which induces heat release from magnetic nanoparticles located at the tumor site. In this study, SPIONs were produced using the chemical co-precipitation technique combined with hydrothermal treatment to reduce their size dispersibility and increase their crystallinity, which are directly related to their magnetic properties. The size of the SPIONs increased from 9 nm to 20 nm after hydrothermal treatment at 160 °C for 24 h. These NPs exhibit a cubic/rectangular shape with a structure composed of both magnetite and maghemite. Their superparamagnetic behavior was confirmed, and the magnetic saturation increased from 58 to 73 emu g^{-1} at RT and from 67 to 81 emu g^{-1} at 10 K. Magnetic hyperthermia measurements showed an increase in SAR values from 83 to about 160–200 W g^{-1}, depending on the hydrothermal treatment conditions. Additionally, the exposure of normal and melanoma cells to SPIONs in the presence of an alternating magnetic field leads to a significant reduction in cell viability, with a more pronounced effect in melanoma cells. These results demonstrate the high potential of this synthesis technique for producing SPIONs for cancer treatment *via* magnetic hyperthermia.

1. Introduction

Magnetic nanoparticles (mNPs) are among the most commonly used inorganic nanoparticles for biomedical applications.[1] Particularly, superparamagnetic iron oxide nanoparticles (SPIONs) are mainly investigated as magnetic hyperthermia agents,[2–7] contrast agents for magnetic resonance imaging (MRI),[6,8] and other biomedical applications.[9–13] For these applications, the magnetic properties of SPIONs (*e.g.*, magnetic anisotropy, coercivity) and their composition, structure, morphology, and stability in the physiological environment are critical. Two types of features primarily influence the magnetic properties: finite-size features (due to quantum confinement) and surface effects, which become more relevant as the particle size decreases due to an increase in the ratio of surface atoms to core atoms. For biomedical applications, NPs ranging from 10 to 50 nm are favored since they form a single magnetic domain and exhibit superparamagnetic properties.[14]

SPIONs composed of magnetite – Fe_3O_4 or maghemite – γ-Fe_2O_3 are the most employed mNPs for magnetic hyperthermia applications.[15,16] Superparamagnetism occurs when the size of magnetic materials is decreased below the single domain limit when the coercivity and remanence reach zero, and the magnetic moments can rotate freely and reverse their direction rapidly. Therefore, in the absence of a magnetic field, the net magnetization of the particle is zero.[15] When an alternating magnetic field (AMF) is applied, SPIONs dissipate heat through relaxation loss by Néel and Brownian relaxation mechanisms. The Néel relaxation mechanism is related to magnetocrystalline anisotropy, while the Brownian relaxation mechanism is associated with the fluid's viscosity in which the nanoparticles are suspended.[15]

The magnetic properties and biological interactions of SPIONs are highly dependent on the synthesis method. Consequently, the chosen synthesis method impairs the magnetic

[a] *CENIMAT/i3N, Department of Materials Science, NOVA School of Science and Technology (FCT NOVA), Campus de Caparica, 2829-516 Caparica, Portugal. E-mail: pi.soares@fct.unl.pt*

[b] *C2TN, Department of Nuclear Sciences and Engineering, Instituto Superior Técnico, Universidade de Lisboa. Estrada Nacional 10, ao km 139.7, 2695-066 Bobadela LRS, Portugal*

[c] *CENIMAT/i3N, Department of Physics, NOVA School of Science and Technology (FCT NOVA), Campus de Caparica, 2829-516 Caparica, Portugal*

hyperthermia efficiency of SPIONs. Many studies have tried to optimize the synthesis method and study the critical parameters that enable fine-tuning diameter, shape, and composition. Chemical co-precipitation of metal salts is the typical synthesis method to produce SPIONs for biomedical applications.[17] Despite the clear advantages of this technique (low cost, green chemistry, high yield, and easy scalability), there is poor control of the size distribution of SPIONs. Resovist® is composed of SPIONs produced by chemical co-precipitation technique and was approved in 2001 in Europe as an MRI contrast agent.[1] However, this formulation's specific absorption rate (SAR) values (typically used to evaluate the efficiency of mNPs in magnetic hyperthermia applications) are low.[18]

Other standard techniques include solvothermal synthesis and thermal decomposition. However, these methods' yields are usually low (milligram scale), they use organic solvents, and the obtained mNPs possess a hydrophobic surface, requiring further processing for biomedical applications.[18] SAR values are usually significantly higher when non-hydrolytic methods are used, although, in most cases, the $H \times f$ product highly surpasses the biological limit (5×10^9 A ms^{-1}) defined by Hergt et al.[19] Thermal decomposition and solvothermal methods produce higher SAR values (4- and 3-fold increase compared to Resovist, respectively). Additionally, these methods enable the production of anisotropic nanoparticles. In some studies, these anisometric-shaped NPs showed a 20 to 30-fold increase in SAR value compared to Resovist.[18]

In this sense, research has been focused on green chemistry methods to synthesize SPIONs through an environmentally friendly approach. Here, a compromise must be found to generate SPIONs with high crystallinity and large magnetic volume by minimizing the thickness of the spin-disordered surface layer.[20] Additionally, the size and shape of the nanoparticles have a strong influence on their magnetic properties. For example, sphere-like SPIONs have lower coercivity compared to cube-like SPIONs, which may be caused by strong exchange interactions during spin alignment.[21]

Hydrothermal synthesis is a hydrolytic synthesis method to produce SPIONs, amongst other inorganic nanoparticles, in which a substance is crystalized in a sealed container (autoclave) at high temperature (typically above 100 °C) and high vapor pressure (typically above 1 atm). In this method, magnetic NPs are produced by rapid nucleation and fast growth, leading to highly crystalline iron oxide nanoparticles. Hydrothermal synthesis is performed through simple, cost-effective experimental procedures, and the obtained NPs exhibit excellent water dispersibility.[22–25] Bonvin et al.[20,26] explored the combination of chemical co-precipitation technique with hydrothermal treatment to improve the particle size dispersibility, morphology, and composition. Additionally, they verified that the size of SPIONs increased from 8 to 21.5 nm with hydrothermal treatment duration (from 0 h to 24 h). Magnetic hyperthermia studies were also conducted under an AMF of 23.9 kA m^{-1} at frequencies ranging from 200 to 600 kHz, showing an increase in SAR with particle size (and, therefore,

hydrothermal treatment duration) for constant frequency and magnetic field strength.

Ozel et al.[27] also studied the effects of hydrothermal treatment duration and temperature after chemical co-precipitation on SPIONs characteristics. The hydrothermal treatment ranged from 1 to 120 hours at 160 °C, showing an increase in particle size from 14 to 74 nm and an increase in saturation magnetization from 74.9 to 93.5 emu g^{-1}, respectively. The particle size distribution was also observed to broaden with increasing reaction time. Torres-Gómez et al.[28] conducted a study to investigate the impact of the synthesis temperature on the shape of NPs. The NPs were synthesized using the hydrothermal method at temperatures of 120, 140, and 160 °C for 4 hours. Morphological analysis revealed NPs with a high degree of crystallinity and distinct shapes at each temperature, specifically quasi-spheres (at 120 °C), octahedrons (at 140 °C), and cubes (at 160 °C). Particle size increased with increasing reaction temperature from 23.46 nm (at 120 °C) to 107.21 nm (at 160 °C). Moreover, magnetic measurements revealed that the saturation magnetization increased with temperature from 52.71 emu g^{-1} at 120 °C to 107.57 emu g^{-1} at 160 °C.

This study combines our previously optimized chemical co-precipitation technique[2,4,6,29] with hydrothermal treatment at 140 °C and 160 °C, testing different treatment durations. In addition, to complete the characterization of the obtained SPIONs to evaluate their morphology, size, and size distribution, the effect of hydrothermal treatment on the magnetic properties (namely magnetic saturation and coercivity) and on magnetic hyperthermia application (namely SAR) was also assessed. Furthermore, it is shown that SPIONs with the best performance induce cell death in normal and tumorous cell lines, using melanoma as a model disease. The cytotoxicity of SPIONs in the absence and presence of an alternating magnetic field were tested to evaluate the potential of these SPIONs for magnetic hyperthermia application in cancer treatment.

2. Experimental section/methods

2.1. Materials

Iron chloride hexahydrate (FeCl$_3$·6H$_2$O, 97%, Alfa Aesar, Ward Hill, MA USA), iron chloride tetrahydrate (FeCl$_2$·4H$_2$O, 98%, Alfa Aesar, Ward Hill, MA USA), ammonia solution (NH$_4$ at 25% in water, Panreac, Chicago IL, USA), and ultrapure water (Millipore, Burlington, MA USA) were used to synthesize iron oxide nanoparticles. Iron quantification using the phenanthroline method[30] was performed using hydrochloric acid (HCl, 37% (v/v), Sigma-Aldrich, St. Louis, MO USA), hydroxylamine (99%, Sigma-Aldrich, St. Louis, MO USA), 1,10-phenantroline (Alfa Aesar, Ward Hill, MA USA), and ammonium acetate (Scharlau, Barcelona, Spain). For in vitro assays, the following materials were used: Dulbecco's modified Eagle's medium low glucose (DMEM-LG, Biowest, Nuaillé, France), DMEM high glucose (DMEM-HG, Biowest, Nuaillé, France), fetal bovine serum (FBS, Biowest, Nuaillé, France) penicillin (100 U mL^{-1}, Invitrogen, Waltham, MA USA), streptomycin (100 μg mL^{-1},

Invitrogen, Waltham, MA USA), gentamicin (10 mg mL^{-1}; Gibco, Waltham, MA USA), amphotericin B (Fungizone®, Quimigen, Alverca do Ribatejo, Portugal), dimethyl sulfoxide (DMSO, Supelco, St. Louis, MO USA), penicillin/streptomycin (P/S, Gibco, Waltham, MA USA), resazurin (Alfa Aesar, Ward Hill, MA USA), phosphate buffer solution (PBS 1× pH 7.4), paraformaldehyde 4% (PFA, Sigma-Aldrich, St. Louis, MO USA), potassium hexacyanoferrate(II) trihydrate 4% (VWR chemicals, Radnor, PA USA), and mowiol (Sigma-Aldrich, St. Louis, MO, USA). All the chemicals used were of analytical grade and used without further purification.

2.2. Synthesis of iron oxide nanoparticles

Superparamagnetic iron oxide nanoparticles were produced using the chemical co-precipitation technique previously described.[29] 5 mmol of iron(III) chloride hexahydrate and 2.5 mmol of iron(II) chloride tetrahydrate were dissolved in 50 mL of ultrapure water, followed by the addition of 10 mL of ammonium solution to precipitate the iron oxide nanoparticles. The reaction was conducted under mechanical stirring (600 rotations per minute) and in anaerobic conditions. The reaction was stopped after 5 minutes by adding 50 mL of ultrapure water. The magnetic precipitate was washed five times with ultrapure water and stored at 4 °C for further use. SPIONs without further treatment were named "pristine NPs". The hydrothermal treatment was performed according to previous literature.[27] Following the chemical co-precipitation synthesis, after the reaction with ammonium solution for five minutes, the alkaline suspension was transferred to a stainless steel autoclave containing a Teflon cup (Parr Instrument Company, model 4748). The autoclave was submitted to 140 °C or 160 °C during different reaction times: 2, 8, 16 and 24 h. After the predetermined time, the autoclave was cooled to room temperature. The resultant precipitate was washed five times with ultrapure water. These NPs were named "X °C Y h" where X corresponds to temperature and Y corresponds to the hydrothermal treatment duration. The iron content of the prepared samples was measured through the 1,10-phenantroline colorimetric method previously described.[30] The relationship between iron and iron oxide NP concentrations was determined using the formula [Fe] = 0.7 × [NPs], obtained from control experiments.[31] A part of the nanoparticle's suspension was freeze-dried (VaCo2, Zirbus) to obtain dry NPs for further characterization.

2.3. Characterization

XRD diffraction (XRD) patterns of dry samples were obtained using the X'Pert PRO PANAlytical X-ray diffractometer. 2θ values were taken from 15° to 80° using a Cu-Kα radiation ($\lambda = 1.54060$ Å) with a step size of 0.033. Scherrer's equation and Williamson–Hall method were used to measure the average crystallite size. Lattice parameters were calculated through interplanar distances determined from the Bragg equation ($\lambda = 2d\sin\theta$).

Transmission electron microscopy (TEM) images were obtained using a Hitachi H-8100 II with thermo-ionic emission

LaB6 with a resolution of 2.7 Å. TEM analysis was performed in NPs diluted in ultrapure water placed in a Kevlar 25 mesh grid. FTIR spectra of the iron oxide nanoparticles were acquired using a Nicolet 6700–thermo electron corporation attenuated total reflectance Fourier transform infrared spectrometer (ATR-FTIR). Measurements were performed in dry samples in the range of 400–4000 cm^{-1} with a resolution of 2 cm^{-1}. Thermogravimetric analysis (TGA) was obtained using a Thermal Analyzer NETZSCH STA 449 F3 Jupiter at a rate of 10 °C min^{-1} (25 to 900 °C) in a N$_2$ atmosphere. Dynamic light scattering (DLS) measurements were performed using a SZ-100 nanoparticle series (Horiba, Lda) with a 532 nm laser and a Peltier temperature control system (25 °C). DLS measurements were carried out for diluted NPs suspensions (five replicas for each concentration) using a disposable cell with a scattering angle equal to 90°. Data analysis was performed using cumulant statistics to measure hydrodynamic diameter (D_H) and polydispersity index (PI).[6] Measurements were performed in fresh samples and after a storage period of 1 month in ultrapure water and DMEM HG. The zeta potential of diluted SPIONs suspension (0.15 mg mL^{-1}) with pH in the range of 6.5 to 8.5 was measured using a graphite disposable cell. The magnetic properties of SPIONs were performed using a 7 T SQUID (superconducting quantum interference device) magnetometer S700X from Cryogenic Ltd (London, UK). Samples of about 10 mg were prepared and inserted in gelatine capsules. The zero field cooled (ZFC) and field cooled (FC) measurements were performed by cooling the sample to 10 K at zero field or in the presence of an external field of 100 Oe, respectively. Isothermal magnetization curves were obtained for fields up to 5 T for 10 and 300 K temperatures.

2.4. Magnetic hyperthermia assays

Magnetic hyperthermia studies were conducted for 10 minutes using a D5 series (Nb Nanoscale Biomagnetics), where 1 mL of NPs solutions was submitted to an AMF with an intensity of 24 kA m^{-1} and frequency of 388.4 kHz. To evaluate the heating ability of the SPIONs, the measurements were performed in 1 mL samples with different NP concentrations diluted in ultrapure water: 1, 2.5, 5, and 10 mg mL^{-1}. After one month, measurements were also made to evaluate stability, keeping the iron concentration at 5 mg mL^{-1}. To mimic a cellular environment, the hyperthermia capability was also tested for NPs ([NPs] = 5 mg mL^{-1}) in PBS 7.4 and DMEM HG, in fresh samples and after one month. Magnetic hyperthermia measurements were also conducted in NPs incubated for 24 hours with HFFF-2 and melanoma cells and about 45×10^4 and 50×10^4 cells were seeded, respectively, for each 1 mL sample. For these measurements, the alternating magnetic field was applied for approximately 4 minutes until 43.5 °C was reached, turned off until it was cooled to 43 °C, and turned on again until 44 °C was attained, for 4 cycles. It should be noted that the equipment has an associated delay, which means the NPs continue to heat up slightly after the magnetic field is turned off and vice versa.

2.5. Cytotoxicity assays

SPIONs samples cytotoxicity was evaluated according to standard ISO-10993 biological evaluation of medical devices, part 5: tests for *in vitro* cytotoxicity. The assays were performed using the direct method, human Caucasian fetal foreskin fibroblast cells HFFF2 (European collection of authenticated cell cultures (ECACC) 86031405) and advanced cutaneous melanoma cancer cells WM983b (Rockland). HFFF2 cell line, representing healthy cells, and WM938b cancer cell line were seeded in 96-well plates at a density of 7.5×10^4 cells mL^{-1}, and 1×10^5 cells mL^{-1}, respectively. HFFF2 cells were grown in DMEM-LG supplemented with 10% FBS and 1% P/S, and WM983b cell line was grown in DMEM-HG supplemented with 5% heat-inactivated FBS and 1% P/S. The plates were seeded and incubated (Sanyo MCO19AIC) overnight at 37 °C in 5% CO_2. A 500 μL solution was prepared, containing concentrations of nanoparticles ranging from 1 to 0.0625 mg mL^{-1}, diluted in the appropriate culture medium with 0.5 μL of gentamicin (10 mg mL^{-1}). Medium was replaced in each well with 100 μL of the NPs suspension in quadruplicates, and the plates were incubated for 24 hours. The negative control cells were never exposed to the NPs solution and the positive control cells were treated with 10% DMSO to induce cell death. The wells were then washed twice with culture medium, and 150 μL of a mixture of resazurin and culture medium (1 : 1) were added to each well and left to incubate for 2 hours. Afterward, 100 μL of each well was placed in another 96-well plate, and the absorbance was measured at 570 nm (absorption peak for resorufin) and 600 nm (absorption peak for resazurin) in a plate reader (Biotek ELX 800 UV). Cell viability was calculated using the conversion of resazurin into resorufin by the negative control cells as the reference.

An identical approach was used to evaluate the cell viability in experiments conducted on cells with NPs that were subjected to magnetic hyperthermia. For comparison purposes, a nanoparticle control was also established where cells were exposed to the same amount of NPs but not subjected to the AMF. Cell control, where cells were not exposed to NPs or to the alternating magnetic field, was also defined. In these experiments, instead of using a 96-well plate initially, the procedure was carried out in the 1 mL flasks used in magnetic hyperthermia.

2.6. Internalization studies

Prussian blue staining was used to visualize iron oxide nanoparticles due to the formation of a bright blue precipitate (ferric ferrocyanide – $(Fe_4^{III}[Fe^{II}(CN)_6]_3)$) when ferric irons react with potassium ferrocyanide $(K_4[Fe(CN)_6]\ 3H_2O)$.[32] HFFF-2 and melanoma cells were seeded in 24-well plates at a density of 22.5×10^4 cells mL^{-1}, and 3×10^5 cells mL^{-1}, respectively, in triplicates for each type of SPIONs and incubated at the previously mentioned conditions. A 0.1 mg mL^{-1} nanoparticle solution was prepared with 2 μL of gentamicin, and 500 μL was placed in each well and left to incubate for 1, 6, and 24 hours, each time point in a distinct plate. The negative control cells were never exposed to the NPs solution. After the respective time points, cells were washed two times with PBS 1×, fixed with PFA 4% for 15 minutes, and stained with a mixture of HCl 4% and potassium hexacyanoferrate(II) trihydrate 4% (1 : 1), diluted in ultrapure water, for 40 minutes. After washing twice more with PBS, cells were then mounted with mowiol and coverslipped. After drying overnight, cells were examined using a microscope (Nikon Eclipse Ti-S with Nikon D610 camera).

2.7. Statistical analysis

In different tests, a statistical study was carried out. For this, at least 3 replicates of each sample and assay were performed. A single-factor analysis of variance (ANOVA) was carried out. Then, a series of statistical parameters were calculated, including the mean and standard deviation. In addition, a mean comparison test was performed to detect significant differences (a confidence level of 95%, $p < 0.05$).

3. Results and discussion

3.1. Structural and morphological characterization

Superparamagnetic iron oxide nanoparticles were produced using the chemical co-precipitation technique. This method enables the production of hydrophilic nanometric nanoparticles with a high yield and adequate superparamagnetic properties for magnetic hyperthermia application. However, their stability in physiological conditions can compromise their biomedical application.[29] Using surfactants or other stabilizing molecules may increase their stability in physiological conditions but usually affect their magnetic saturation and performance in magnetic hyperthermia applications. Combining chemical co-precipitation synthesis with hydrothermal treatment makes it possible to enhance the stability and magnetic saturation of SPIONs, without stabilizing molecules.[20,27]

SPIONs structural characterization was performed before (pristine NPs – without hydrothermal treatment) and after hydrothermal treatment (X °C Y h, where X corresponds to the temperature and Y corresponds to the hydrothermal treatment duration – 2, 8, 16, and 24 h). XRD patterns of the corresponding samples are displayed in Fig. 1A. The obtained patterns were compared to standard diffraction patterns of magnetite (JCPDS 039-1346) and maghemite (JCPDS 019-629). All peak positions at (2 2 0), (3 1 1), (2 2 2), (4 0 0), (4 2 2), (5 1 1), (4 4 0), and (5 3 3) are consistent with the standard X-ray data for magnetite or maghemite. All samples display a crystalline cubic structure. Comparing pristine NPs with samples submitted to hydrothermal treatment, it is visible that the diffraction peaks become sharper with the increase of hydrothermal treatment time, indicating a crystallinity enhancement.[27,33] The most significant difference is observed in pristine NPs, where a smaller peak definition is observed compared to samples with hydrothermal treatment. Samples submitted to a hydrothermal treatment longer than 16 h (inclusive) have a higher degree of crystallinity, also showing the presence of a diffraction peak (2 2 2) that is not visible in other samples.
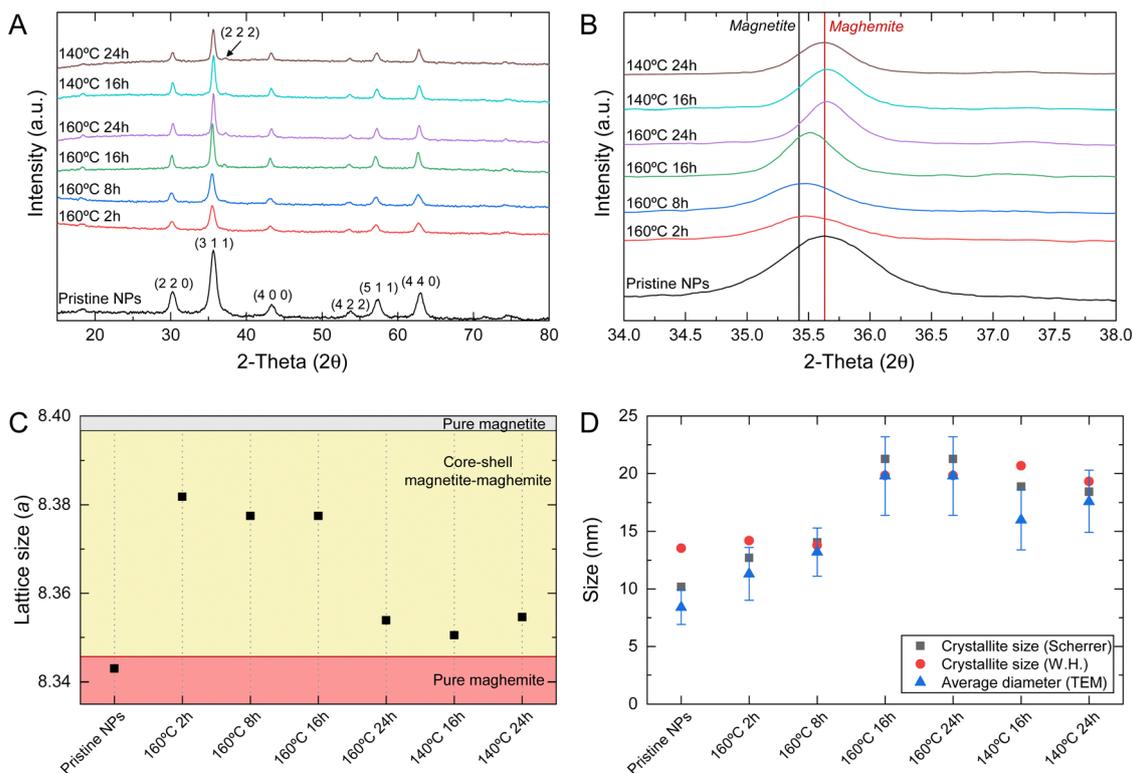
Fig. 1 (A) XRD diffractogram and respective (B) magnification of the most intense peak (3 1 1) of pristine NPs produced by chemical co-precipitation technique without further treatment, and SPIONs that underwent hydrothermal treatment under different temperature and duration conditions. (C) Calculated lattice parameter (*a*) based on the XRD data and the respective correspondence to pure magnetite (gray zone), pure maghemite (reddish zone), and core−shell magnetite−maghemite (yellowish zone). (D) Comparison of calculated crystallite size using the Debey−Scherrer equation and the Williamson−Hall (W. H.) method, and the average diameter measured on TEM data.

Magnetite typically precipitates in an inverse spinel structure with oxygen atoms organized in a closed-packed cubic lattice containing iron(III) atoms in the tetrahedral sites and a mixture of iron(II) and iron(III) atoms in the octahedral sites. Since iron(II) is highly unstable in air, magnetite usually oxidizes partially or entirely into maghemite. This oxidation may result in core–shell magnetite–maghemite NPs or pure maghemite NPs, respectively.[34]

Since magnetite and maghemite present similar XRD patterns with discrete differences, a simple comparison with standard diffraction patterns is insufficient to distinguish between these iron oxide specimens. A closer evaluation of the highest intensity peak (3 1 1) of XRD patterns (Fig. 1B) demonstrated that pristine NPs obtained by traditional chemical co-precipitation technique have a peak position closer to that of pure maghemite (2θ = 35.631). The hydrothermal treatment at 160 °C below 16 h originates NPs with a peak position closer to pure magnetite (2θ = 35.423). However, a hydrothermal treatment longer than 16 h (at 140 °C or 160 °C) leads to NPs with peak positions closer to pure maghemite. Additionally, the lattice parameter is slightly different for magnetite (8.3967 Å) and maghemite (8.3457 Å).[34] A more detailed analysis of peak broadening that can influence the distance between adjacent planes (*d*) calculated by the Bragg eqn (1):

$$\lambda = 2d \sin \theta \tag{1}$$

Where θ is the diffraction angle, and λ is the incident X-ray wavelength. The lattice parameter (*a*) of each sample was calculated using (2):

$$\frac{1}{d_{hkl}^2} = \frac{h^2 + k^2 + l^2}{a^2} \tag{2}$$

Where (*h k l*) corresponds to Miller indices of the higher intensity peak (3 1 1). Fig. 1C represents the calculated lattice parameter of each sample and their correspondence to the intervals of lattice parament of pure magnetite and maghemite found in the literature.[34] The data obtained suggests that pristine NPs are indeed composed of maghemite, which may be a result of post-synthesis oxidation of NPs since they are stored in ultrapure water in the presence of air. When the hydrothermal treatment is performed at 160 °C during 2 h, 8 h, and 16 h, the NPs experience a lattice size increase, possibly related to a size-dependent lattice expansion.[34] However, performing the same hydrothermal treatment for 24 h leads to a smaller rise in lattice parameters. The same effect is observed with the hydrothermal treatment performed at 140 °C for 16 h and 24 h. In the later samples, a lattice contraction driven by oxidation[34] may come into play, leading to NPs composed mainly of maghemite and a smaller lattice parameter compared

to smaller durations of hydrothermal parameters. Previous reports demonstrate that oxidation of iron(II) during the hydrothermal treatment may occur since the reaction occurs in the presence of oxygen.[35]

Additionally, peak broadening analysis allows the calculation of crystallite size and lattice strain. The average crystallite size (D) is inversely proportional to the full width at half-maximum (β) of the highest intensity diffraction peak (3 1 1), and was calculated through the Debye–Scherrer eqn (3):

$$D = \frac{K\lambda}{\beta \cos \theta} \quad (3)$$

Where K is the shape factor (0.94).[29,36] The average crystallite size (Table 1) of the untreated sample is 10.2 nm, increasing to 12.7, 14.1, 20.6, and 21.3 nm with 2, 6, 16 and 24 h of hydrothermal treatment at 160 °C, respectively. At 140 °C, the average crystallite size is 18.9 and 18.4 nm for 160 h and 24 h hydrothermal treatment, respectively. The size increase is caused by the redissolution of smaller disfavored NPs nuclei, followed by their deposition onto larger nuclei, which are more thermodynamically favorable. This particle growth pathway is called the Ostwald ripening pathway.[37]

Since the Debye–Scherrer equation only attributes peak broadening to crystallite size, it usually underestimates the average crystallite size. Alternatively, Williamson–Hall analysis can distinguish the independent contributions of crystallite size and lattice strain to peak broadening. Additionally, in this analysis, all visible diffraction peaks are considered. Using (4), the crystallite size (D) can be estimated from the y-intercept and lattice strain (ε) from the slope of the linear fit to the data.

$$\beta_T \cos \theta = \frac{K\lambda}{D} + 4\varepsilon \sin \theta \quad (4)$$

Eqn (4) is dependent on the diffraction angle. The Williamson–Hall method does not depend on $(1/\cos \theta)$; instead, it varies with $\tan \theta$. Therefore, the Williamson–Hall method can distinguish the contribution of crystallite size and lattice strain to Bragg peak broadening.[33] A precise crystallite size can be determined by (5):

$$\beta_T \cos \theta = \frac{K\lambda}{D} + \varepsilon(4 \sin \theta) \quad (5)$$

This equation represents the uniform deformation model, where the lattice strain is considered constant in all crystallographic directions, i.e., considering an isotropic nature of the crystal. If the term ($\beta_T \cos \theta$) is plotted with respect to ($4 \sin \theta$), the lattice strain and crystallite size can be obtained from the slope and y-intercept, respectively. Table 1 shows the results obtained, where it is visible that in most cases, the crystallite size obtained through the Williamson–Hall method is higher than the one obtained by the Scherrer equation, which is in accordance with previous publications.[33,36] An exception is seen in samples 160 °C 8 h, 16 h, and 24 h, where the crystallite size estimated by the Williamson–Hall method is smaller, which may be caused by the lattice shrinkage effect.[33]

As expected, an increase in crystallite size is also visible with the increase of hydrothermal treatment duration.[20] The Ostwald ripening mechanism can explain this size increase. This mechanism is significant when the precursor concentration (in this case, iron(II) and iron(III)) decreases to levels below the nucleation threshold. At that stage, small nuclei energetically disfavored redissolve and deposit in larger nuclei, which is thermodynamically favorable, thus producing larger particles.[37] Increasing the reaction time from 16 h to 24 h does not significantly increase the crystallite size.

TEM evaluated the morphology of the prepared iron oxide NPs. Fig. 2 exhibits the representative images of each sample and the respective size distribution graph obtained from at least 150 measurements. Similarly to what was observed in the crystallite size, there is a size enlargement associated with the increase of hydrothermal treatment duration, pristine NPs have an average size of 9.3 nm, which increases to 11.3, 13.2, 17.6, and 19.8 nm when the hydrothermal treatment is applied at 160 °C for 2 h, 8 h, 16 h, and 24 h, respectively. At 140 °C, the NPs size increases to 16.0 and 17.6 nm for a treatment duration of 16 h and 24 h, respectively (Table 1). These results are in agreement with the literature, where it is demonstrated that at higher temperatures, the reaction duration has a more significant impact on particle size.[27]

Additionally, the hydrothermal treatment induces a change in NPs morphology: while pristine NPs present a quasi-spherical shape, NPs undergoing hydrothermal treatment have a cubic/rectangular shape with more faceted edges (Fig. 2E–H). During synthesis, NPs adapt to the most thermodynamically stable morphology. Following growth processes like Ostwald ripening and coalesce, NPs recrystallize and reveal lower energy surfaces. This is in accordance with the Gibbs–Wulff theorem, which states that a crystal will rearrange itself to minimize surface energy by taking on a shape depending on its preferred growing planes.[38] In magnetite's face-centered cubic (FCC) structure, the most stable, i.e., lower energy, crystallographic facet $\langle 1\,1\,1 \rangle$, followed by $\langle 1\,0\,0 \rangle$, which leads magnetite-based NPs to acquire an octahedral shape, which leads to a quasi-sphere form when truncated. NPs will increase in size and maintain their shape if the facets grow at the same rate. If one of the facets has lower energy, it expands due to increased growth in the perpendicular direction of higher-energy surfaces.[28,39]

Table 1 Average TEM diameter, crystallite size determined by the Debye–Scherrer equation and the Williamson–Hall method, lattice strain obtained by Williamson–Hall method, and lattice parameter obtained by the Bragg equation

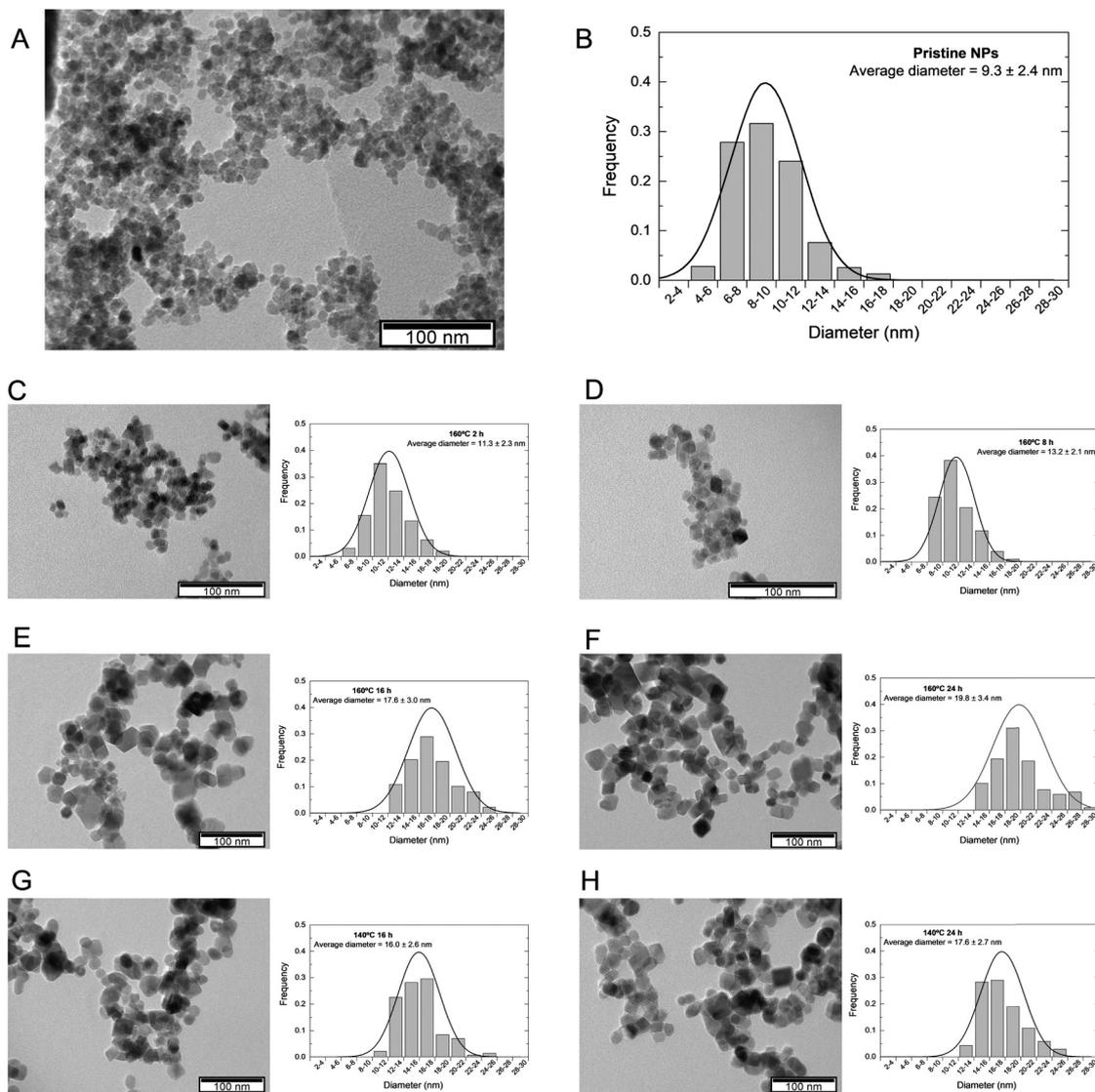|	TEM diameter (nm)	Crystallite size (nm)		Lattice strain	Lattice parameter (Å)
		Debye–Scherrer	Williamson–Hall		
Pristine NPs	9.3 ± 2.4	10.7	11.3	−0.0012	8.3484
160 °C 2 h	11.3 ± 2.3	12.7	14.2	−0.0009	8.3818
160 °C 8 h	13.2 ± 2.1	14.1	13.8	−0.0002	8.3775
160 °C 16 h	17.6 ± 2.5	20.6	20.4	−0.0007	8.3775
160 °C 24 h	19.8 ± 3.4	21.3	19.8	−0.0004	8.3539
140 °C 16 h	16.0 ± 2.6	18.9	20.7	−0.0004	8.3505
140 °C 24 h	17.6 ± 2.7	18.4	19.3	−0.0007	8.3546

Fig. 2 (A) Representative TEM images and the respective (B) size distribution graph obtained from at least 150 measurements of pristine NPs obtained from chemical co-precipitation technique without further treatment, and SPIONs subjected to a hydrothermal treatment of 160 °C 2 h (C), 160 °C 8 h (D), 160 °C 16 h (E), 160 °C 24 h (F), 140 °C 16 h (G), and 140 °C 24 h (H).

Taking this into consideration, it appears that for the synthesized SPIONs with hydrothermal treatment, facet ⟨1 0 0⟩ became more stable, leading to more intense perpendicular growth to facet ⟨1 1 1⟩ and thus resulting in a cubic shape. After these processes occur, NPs tend to recrystallize and expose lower energy surfaces. The occurrence of a polyhedral shape in SPIONs submitted to or prepared by the hydrothermal method has already been reported in other research studies, such as Gómez *et al.*, who observed a cubic shape for NPs synthesized at 160 °C and an octahedral structure for 140 °C.[28]

Except for pristine NPs, all samples exhibited a highly similar size between the particle size estimated by TEM and the crystallite size determined by XRD, as seen in Table 1. SPIONs that underwent hydrothermal treatment seem to have a single coherently diffracting (crystallite) domain.[36] Accordingly, SPIONs' size evolution concerning the hydrothermal treatment

conditions appears to follow the same pattern as crystallite size, suggesting that size increased with hydrothermal treatment duration and temperature. It is worth noting that the most similar results are those of SPIONs that underwent hydrothermal treatment at 160 °C for 16 hours and 140 °C for 24 hours, implying that the temperature difference compensates for the duration difference and *vice versa*, resulting in similar-sized SPIONs.

DLS measurements were performed to evaluate the prepared NPs' hydrodynamic diameter and their behavior and stability in simulated *in vivo* conditions (culture medium). Additionally, DLS measurements also determine the polydispersity index (PI), providing insight into the size heterogeneity of the sample. Long-term colloidal stability in water was evaluated by carrying out these measurements immediately after synthesis and again after a storage period of one month at 4 °C. The assessment of

size and colloidal stability of NPs is of utmost importance in therapeutic applications, as these characteristics significantly impact their mechanism of action in both *in vitro* and *in vivo* environments.[40] The correlation function was fitted considering a polydisperse sample with two decay rates. Consequently, the hydrodynamic diameter calculation revealed two separate size groups: smaller particles (D_{H1}) and aggregates (D_{H2}). The latter was considered insignificant when it comprised less than 20% of the correlation function. The pronounced co-existence of both size groups suggested that the sample is not monodispersed. Furthermore, a PI greater than 0.3 is widely accepted as a clear indicator of broader size distribution, indicating aggregation.[41]

Fig. 3A represents the hydrodynamic diameter of all samples in water immediately after synthesis and after storage in water at 4 °C for one month. The values are also summarized in Table 2. It is visible that in most cases, the NPs present a hydrodynamic size below 200 nm immediately after synthesis, except for sample 160 °C 24 h. The more significant difference between TEM diameter and the hydrodynamic diameter may be related to some degree of aggregation caused by strong magnetic dipole–dipole interactions between particles and the interparticle interactions *via* van der Waals forces.[24] After one month of storage, most samples maintain their hydrodynamic size, except for samples 160 °C 2 h and 8 h. In both cases, the

smaller hydrothermal treatment may lead to incomplete recrystallization of the NPs,[42] which may increase the polydispersity of the sample and the instability of NPs, leading to more aggregates. Indeed, larger hydrodynamic sizes are associated with larger PI, sometimes overcoming the conventional limit of 0.3, indicating a polydisperse sample.[41]

Zeta potential measurements provide a measure of the nanoparticle surface charge. This constitutes a crucial aspect of NPs' physicochemical characterization since it allows for evaluating SPIONs' colloidal stability and correlation to characteristics critical to biomedical applications like toxicity and cellular internalization. Only highly stable NPs that can remain dispersed will be used in therapeutic applications. According to the literature, a stable colloidal system will have a zeta potential above 30 mV (in absolute value).[43,44] Table 2 displays the measured zeta potential values for all samples immediately after synthesis and after one month of storage. The zeta potential value in all samples is below −30 mV, indicating high colloidal stability. After storage, the values were kept in the interval considered stable, although a higher value was exhibited for all samples. This may be related to a rearrangement in the Stern layer, leading to a more negative surface charge at the aggregates of NPs.[45,46]

FTIR spectra of pristine NPs and NPs with different hydrothermal treatments are presented in Fig. 4A, where it is possible
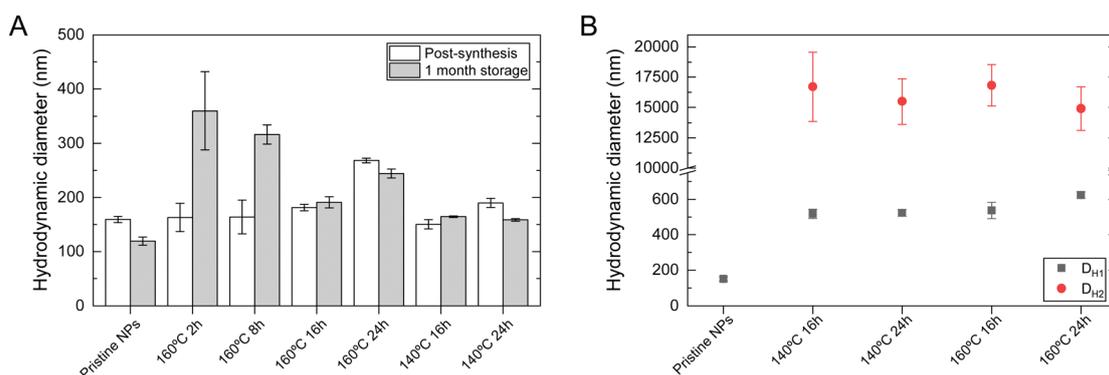

Fig. 3 Dynamic light scattering results: hydrodynamic diameter of pristine NPs obtained from chemical co-precipitation technique without further treatment, and SPIONs subjected to the hydrothermal treatment: (A) in ultrapure water immediately after synthesis, and after one month of storage at 4 °C, and (B) in DMEM HG. D_{H1} and D_{H2} represent the smaller hydrodynamic diameter and large aggregates, respectively, determined using the cumulants method considering a polydisperse sample. Data is expressed as average ± standard deviation for at least five independent experiments.

Table 2 Dynamic light scattering results: hydrodynamic diameter (D_H), polydispersity index (PI), and zeta potential (zeta) obtained immediately after synthesis and after one month of storage at 4 °C of pristine NPs obtained from chemical co-precipitation technique without further treatment, and SPIONs subjected to the hydrothermal treatment at different temperatures and durations

|	Post-synthesis			1-Month storage		
	D_H (nm)	PI	Zeta (mV)	D_H (nm)	PI	Zeta (mV)
Pristine NPs	159 ± 6	0.186 ± 0.089	−33.1 ± 0.6	119 ± 7	0.205 ± 0.063	−50.5 ± 1.7
160 °C 2 h	163 ± 26	0.285 ± 0.048	−43.5 ± 1.1	360 ± 72	0.285 ± 0.095	−41.8 ± 0.2
160 °C 8 h	164 ± 31	0.313 ± 0.039	−36.4 ± 0.7	316 ± 18	0.343 ± 0.081	−34.6 ± 0.9
160 °C 16 h	181 ± 6	0.202 ± 0.033	−39.5 ± 0.2	191 ± 10	0.236 ± 0.054	−59.2 ± 3.6
160 °C 24 h	268 ± 4	0.258 ± 0.035	−37.8 ± 4.7	244 ± 8	0.315 ± 0.048	−54.6 ± 5.8
140 °C 16 h	150 ± 8	0.219 ± 0.062	−31.1 ± 4.7	164 ± 2	0.170 ± 0.022	−62.4 ± 2.5
140 °C 24 h	190 ± 8	0.256 ± 0.074	−32.3 ± 4.2	159 ± 2	0.221 ± 0.034	−58.2 ± 0.5
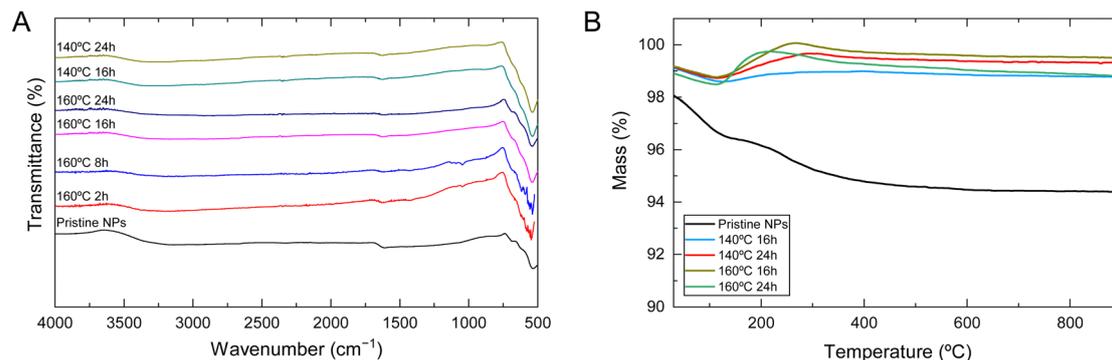
Fig. 4 (A) FTIR spectra and (B) thermogravimetric analysis of pristine NPs obtained from chemical co-precipitation technique without further treatment, and SPIONs subjected to the hydrothermal treatment at 140 °C or 160 °C during 2 h, 8 h, 16 h, or 24 h.

to identify transmittance bands characteristic of iron oxide. At 570 cm^{-1}, the band is associated with the Fe–O stretching mode of the tetrahedral and octahedral sites, representing a typical magnetite absorption band. This is observed for all samples; however, it is substantially weakened for pristine SPIONs compared to the others. According to Ercuta *et al.*,[47] a narrow band at 570 cm^{-1} suggests high purity and a lack of defects, features that appear to increase with the intensity of the hydrothermal treatment. The band at 1630 cm^{-1} is associated with the H–O–H stretching vibration mode and seems to narrow and sharpen in the same manner as the previously mentioned band. The final broader band (3000 to 3400 cm^{-1}) is attributed to the O–H stretching vibration mode due to possible moisture on the sample.[29]

TGA and DTA analysis was performed to evaluate the thermal stability and composition of the NPs. TGA curves for all synthesized NPs are presented in Fig. 4B. The initial weight loss until 120 °C can be associated with the evaporation of residual water on the sample, which accounts for less than 1%, except for pristine NPs, which is 1.88% (still very residual). From that temperature forward, a distinct difference exists between pristine NPs and NPs that underwent hydrothermal treatment. Pristine NPs present a further mass loss of 2.02%, which is associated with the conversion of Fe_3O_4 to γ-Fe_2O_3 and FeO, which are the stable phase of the diagram of Fe–O system above 570 °C.[48]

The thermogram shows that NPs subjected to hydrothermal treatment exhibit a slight mass gain of about 1%, approximately between 100 and 200 °C. This behavior can be attributed to the oxidation of Fe^{2+}, indicating the transformation of magnetite into maghemite. Previous studies have also confirmed that the oxidation of magnetite leads to a mass gain. Similar findings were reported for magnetic NPs that underwent hydrothermal treatment at 250 °C for 24 hours.[49,50] Upon reaching 500 °C, the NPs' mass stabilizes. Although the differences in mass gain are minimal between the four samples, sample 140 °C 16 h is the one with smaller mass gain (0.36%) compared to 140 °C 24 h (0.94%), 160 °C 16 h (1.29%), and 160 °C 24 h (1.25%). These results agree with the variations in lattice parameters represented in Fig. 1C, in which sample

140 °C 16 h is closer to pure maghemite. Additionally, these results confirm a possible partial oxidation of magnetite during the hydrothermal treatment, which may lead to a possible core–shell magnetite/maghemite NP.[35]

3.2. Magnetic evaluation of iron oxide nanoparticles

Considering the previous results, the applicability of the produced magnetic NPs as magnetic hyperthermia mediators and *in vitro* experiments were only performed on samples subjected to a hydrothermal treatment of 16 h or 24 h. These samples exhibit larger crystallite and TEM sizes, are more stable over time, and have a different morphology than pristine NPs. To evaluate the effect of the hydrothermal treatment, pristine NPs are also included in the following analysis.

The magnetic properties of the produced SPIONs were evaluated through SQUID measurements (Fig. 5). Table 3 summarizes the results obtained concerning the saturation magnetization (M_S), coercivity (H_C), and magnetic remanence (M_r) at 10 K and 300 K. The temperature dependence of the magnetization curve in the zero field cooled (ZFC) and field cooled (FC) states under an applied field of 100 Oe for the different tested samples. The blocking temperature (T_B) was determined as the maximum value of the ZFC curve. It is observed that the ZFC and FC curves only converge at 310 K, suggesting a superparamagnetic behavior for the NPs at this temperature. For pristine NPs, T_B is well below 300 K, which indicates superparamagnetic behavior in physiological conditions. This magnetic behavior is also confirmed by the absence of coercivity and remanence at 300 K. For sample 140 °C 16 h T_B can be only estimated by the broad maximum at approximately 192 K. The curve characteristics of the remaining samples are interestingly dominated by the presence of the Verwey transition at approximately 102 K, which masks the appearance of the T_B maximum. The Verwey transition is usually observed at close to 120 K and is a characteristic property of perfect stoichiometric magnetite particles larger than 20 nm in diameter due to the electron transfer that occurs between the Fe^{2+} and Fe^{3+} cations in the octahedral coordination.[51,52] With the reduction in particle size, the Verwey temperature tends to shift towards lower values.[53–55] Besides the smaller size, for the pristine and the
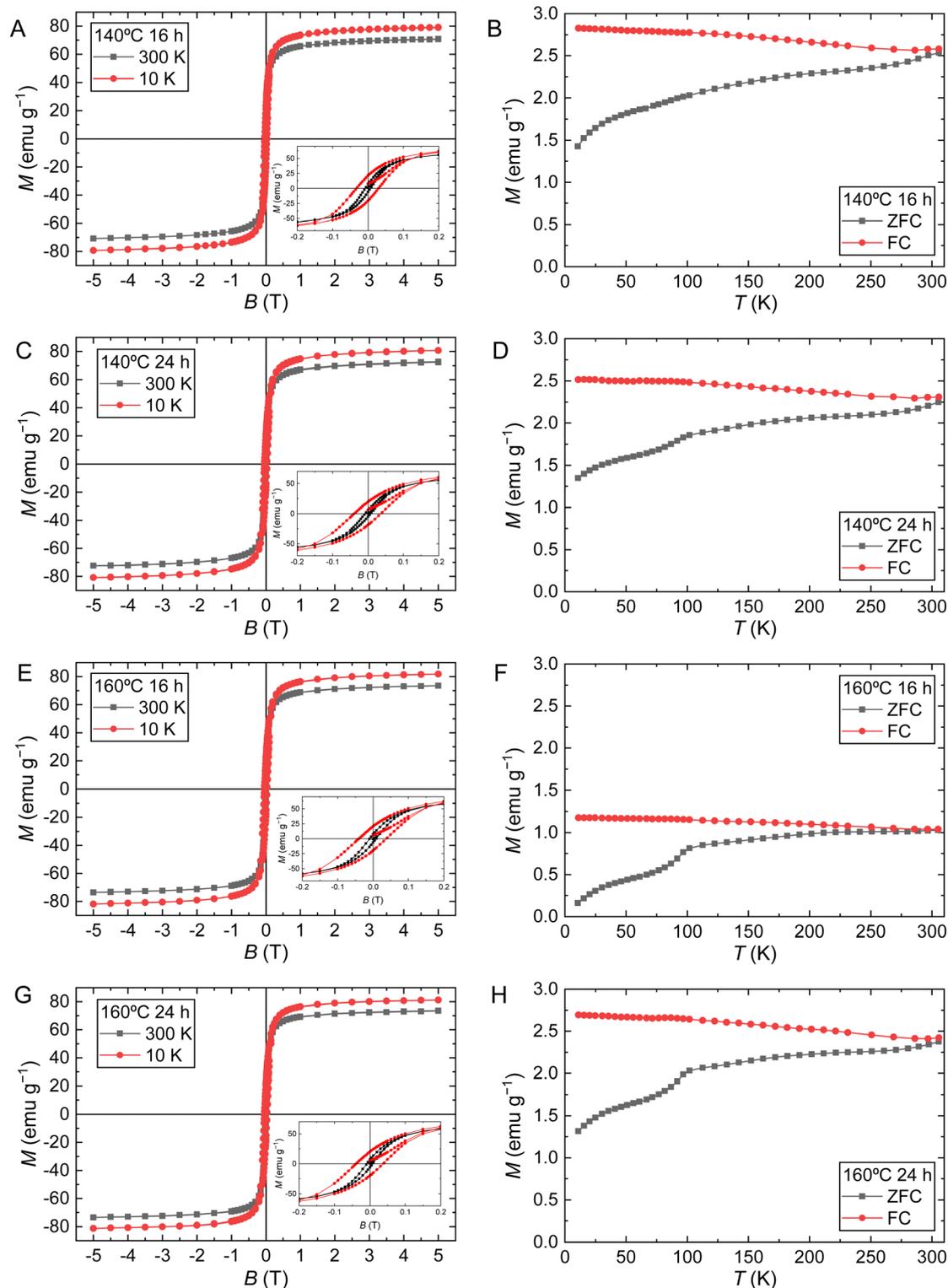
Fig. 5 Magnetic results of SPIONs samples with further hydrothermal treatment: (left) magnetization (M) as a function of the magnetic field (B) at different temperatures and durations at 10 K and 300 K; (right) magnetization (M) as a function of the temperature (T) at a magnetic field of 100 Oe.

140 °C 16 h samples, the Verwey transition may not be observed because nanoparticles are sufficiently non-stoichiometric due to surface effects, such as surface dead layer and oxidation. In fact, samples 140 °C 24 h, 160 °C 16 h, and 160 °C 24 h show

sizes not far from 20 nm (see Table 1). The data in Table 3 indicates that these nanoparticle samples, with the exception of pristine NPs, are still slightly ferrimagnetic in nature at 300 K, showing measured coercivity and remanence values. However,

Table 3 Magnetic properties of pristine NPs and SPIONs with further hydrothermal treatment at different temperatures and durations: saturation magnetization (M_S) at 10 K and 300 K, coercivity (H_C), magnetic remanence (M_r) at 10 K, and blocking temperatures (T_B)

	M_S (emu g^{-1})		H_C (Oe)		M_r (emu g^{-1})		
	10 K	300 K	10 K	300 K	10 K	300 K	T_B (K)
Pristine NPs[29]	67	58	260		16		155
140 °C 16 h	79.2	70.8	300	75	21	7	192
140 °C 24 h	80.7	72.7	380	77	19	5	—
160 °C 16 h	81.8	73.5	390	85	20	7	—
160 °C 24 h	81.2	73.3	380	75	20	7	—

for biomedical applications, these values are negligible as the human body is at a slightly higher temperature of 36.6 °C (312 K), where the behavior of these samples is already superparamagnetic. The M_S values are in good agreement with the literature of synthesized SPIONs through similar methods.[20,35] The increase of M_S after samples being subjected to hydrothermal treatments is certainly due to the observed ferrimagnetic behavior, which corroborates the results from the ZFC/FC magnetic data and may reveal a higher percentage of magnetite, in particular for the sample treated at higher temperatures,

160 °C during 16 h, with higher M_S values of 73.5 emu g^{-1}. These results also agree with the structural data and the increase of the crystallite sizes of treated samples that were found to be higher than those of the pristine NPs.

Magnetic hyperthermia measurements were conducted to evaluate the SPIONs heating ability when submitted to an AMF with a frequency of 388.4 kHz, which falls within the range of preferred frequencies for human applications, typically 100 to 500 kHz.[56] Through the results obtained by TEM, it has been determined that all the synthesized NPs possess a diameter smaller than 30 nm, and by SQUID, these NPs exhibit superparamagnetic behavior at the human body temperature. The temperature variation as a function of the iron concentration for various NPs is illustrated in Fig. 6A. It is observed that the temperature variation increased proportionally with the iron concentration for all samples. However, it was less intense for pristine NPs compared to NPs undergoing hydrothermal treatment. This difference appeared to become more pronounced as the iron concentration increased. SPIONs that underwent hydrothermal treatment increased temperature up to 60 ± 4 °C for hydrothermal treatment at 140 °C for 16 hours at a NPs concentration of 10 mg mL^{-1}, whereas pristine NPs only increased 28 ± 2 °C at the same concentration. No significant
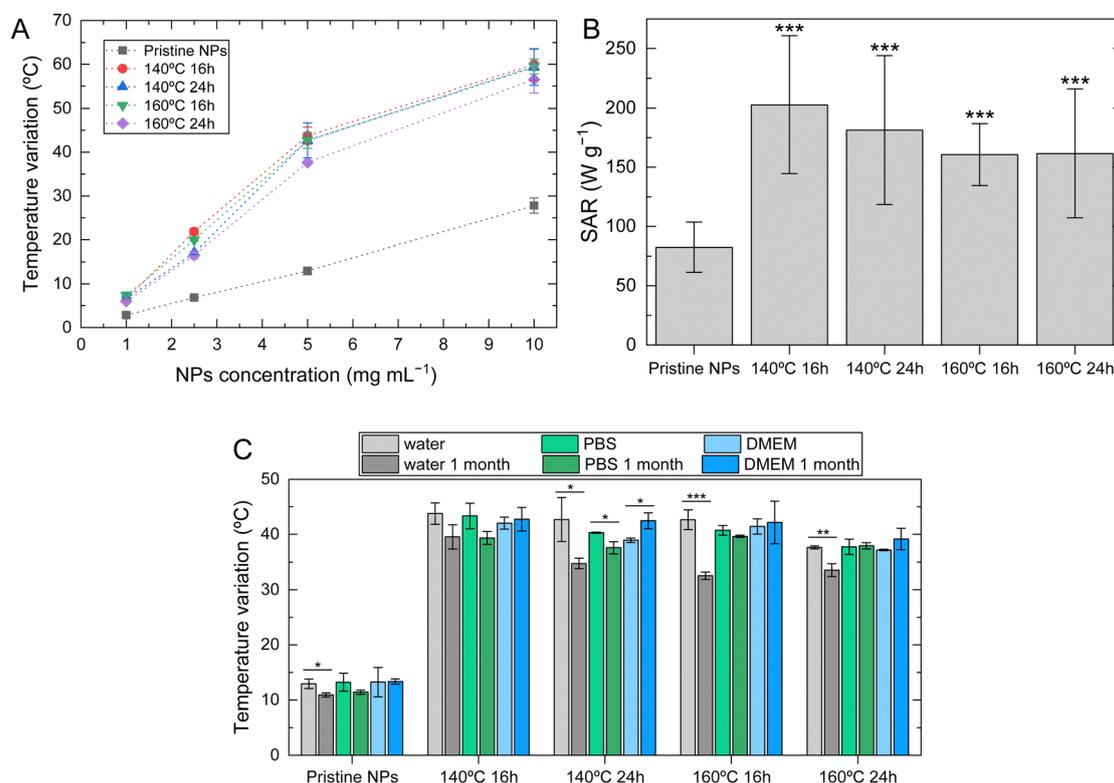

Fig. 6 Magnetic hyperthermia assays performed on pristine NPs, and SPIONs with further hydrothermal treatment at different temperatures and durations. (A) Temperature variation measured during 10 minutes of application of an external alternating magnetic field at an intensity of 24 kA m^{-1} and frequency of 388.4 kHz at different nanoparticle (NP) concentrations. (B) Specific absorption rate (SAR) of freshly prepared samples at a concentration of 5 mg mL^{-1}. (C) Temperature variation of NPs dispersed in water, phosphate buffer solution (PBS 7.4) or DMEM HG at a nanoparticle concentration of 5 mg mL^{-1}; measurements were performed in freshly prepared samples and after a storage time of 1 month at 4 °C. Data is expressed as average ± standard deviation for at least three independent experiments. *$p < 0.05$, **$p < 0.005$, ***$p < 0.001$ compared to pristine NPs (B) or with freshly prepared sample (C).

differences were found between samples that underwent hydrothermal treatment.

A better comparison between samples can be made using the specific absorption rate (SAR), which can be determined using (6):

$$\text{SAR} = \frac{C_{NP}m_{Fe} + C_l m_l}{m_{Fe}} \times \left(\frac{dT}{dt}\right)_{max} \quad (6)$$

where $(dT/dt)_{max}$ is the maximum slope of the colloidal temperature curve submitted to a hyperthermia test, C_{NP} is the specific heat of the nanoparticles, m_{Fe} is the iron mass, C_l is the specific heat of the liquid and m_l is the fluid mass.[6] The maximum slope of the colloidal temperature curve was determined at the first instances after the magnetic field was set to 300 Gauss on all measurements to determine an accurate value of SAR and secure adiabatic conditions.[4]

SAR values are shown in Fig. 6B for all samples at a NP concentration of 5 mg mL^{-1}. Comparing pristine NPs with the ones subjected to hydrothermal treatment, pristine NPs exhibit lower values (82.5 ± 21.2 W g^{-1}). Notably, SPIONs subjected to hydrothermal treatment at 140 °C for 16 hours show the highest SAR value of 203 ± 58 W g^{-1} for the same NP concentration. These differences can be correlated to the previously analyzed morphological characteristics. Typically, SPIONs produced by hydrolytic methods like the chemical co-precipitation technique exhibit low SAR values.[18] It is known that small changes in SPIONs structural characteristics can strongly impact other characteristics, including magnetic ones. An enhanced surface crystallinity is linked to an increased magnetic volume and a reduced magnetically inactive surface layer, leading to a high magnetization saturation and an improved capacity for heat generation. Additionally, the shape of the NP also plays a crucial role in determining its magnetic properties, with cubic-shaped particles exhibiting higher levels of magnetization saturation.[27,28] Bovin et al.[20] demonstrated that with the increase of hydrothermal treatment time, iron oxide NPs may increase their SAR value from approximately 25 W g^{-1} (pristine samples) to approximately 400 W g^{-1} (24 h of hydrothermal treatment). SPIONs subjected to hydrothermal treatment showed higher crystallinity and a cubic shape, which may contribute to the observed results. This highlights the potential of hydrothermal treatment to improve the SAR values of pristine NPs, thus rendering them suitable for magnetic hyperthermia applications.[20] It was observed that SPIONs with different hydrothermal treatment conditions exhibited slight differences in SAR values, which are not statistically significant.

Fig. 6C presents the magnetic hyperthermia results at a NP concentration of 3.5 mg mL^{-1} of freshly prepared NPs, and after one month of storage at 4 °C in ultrapure water, PBS 7.4, or cell culture medium (DMEM HG). When stored in water, all samples exhibit a decrease in the temperature increase and SAR values (Table 4) that can be attributed to the loss of colloidal stability, as Brownian and Néel relaxation are affected by this phenomenon. Nevertheless, the SAR value of all samples remains above 100 W g^{-1} and higher than pristine SPIONs.

Table 4 Magnetic hyperthermia results of pristine NPs, and SPIONs with further hydrothermal treatment at different temperatures and durations: temperature variation (ΔT), specific absorption rate (SAR), intrinsic loss power (ILP), obtained in freshly prepared samples and samples stored during one month at 4 °C. All samples were measured at a nanoparticle concentration of 5 mg mL^{-1}

	ΔT (°C)	SAR (W g^{-1})	ΔT 1 month (°C)	SAR 1 month (W g^{-1})
Pristine NPs	12.9 ± 0.9	82.5 ± 21.2	10.9 ± 0.4	55.6 ± 11
140 °C 16 h	43.8 ± 1.9	203 ± 58	39.5 ± 2.2	113 ± 20
140 °C 24 h	42.7 ± 3.9	181 ± 63	34.8 ± 0.9	165 ± 17
160 °C 16 h	42.7 ± 1.8	161 ± 26	32.5 ± 0.7	144 ± 7
160 °C 24 h	37.6 ± 0.3	162 ± 54	33.6 ± 1.2	157 ± 2

To evaluate the heating efficacy of SPIONs in physiological environment, magnetic hyperthermia measurements were conducted on SPIONs diluted in both DMEM HG and PBS. DMEM exhibits high viscosity and, as a result, significantly affects Brownian motion. However, it does not strongly influence Néel relaxation, which is the reorientation of the magnetic moment within a nanoparticle, independent of physical rotation.[57,58] Therefore, most heat release may be attributable to Néel relaxation in these conditions. Comparing temperature increase values in water, PBS, and DMEM HG, no significant differences are observed. This indicates that, despite the higher viscosity of DMEM HG or the possible interaction of ions/proteins present in PBS and DMEM with the surface of NPs, which may result in NP aggregation, are not affecting the heating ability of NPs. Therefore, heat release is occurring with the contribution of both Brownian and Néel relaxation mechanisms.[56,59]

3.3. In vitro cytotoxicity and internalization

In vitro cytotoxicity assays are critical for evaluating the safety and biocompatibility of NPs in medical applications. The assays were performed using a resazurin assay on fibroblasts (HFFF2 cell line) and melanoma cells (WM938b cell line). These experiments provided insights into the cytotoxicity on both normal and tumor cells at different NP concentrations (Fig. 7). The viability of both fibroblasts and melanoma cells remained consistently high, exceeding 80%, after exposure to varying concentrations of NPs for 24 hours. These results indicate that the synthesized NPs, at concentrations below 1 mg mL^{-1} do not cause toxicity to the studied cell lines. These results are in accordance with the literature, which evaluated the cytotoxicity profile of pristine NPs and NPs treated hydrothermally at 100 and 200 °C on tumor cells.[6,60] No significant differences in cytotoxicity were observed between the hydrothermal conditions or the normal and tumor cell lines.

To develop safe and effective NPs and assess their potential risks for biomedical applications, it is essential to conduct internalization studies to better understand how SPIONs interact with living cells. Furthermore, examining how the morphological changes induced by hydrothermal treatment impact cell uptake is beneficial. Prussian blue staining was used to label SPIONs and obtain internalization images for HFFF2 and
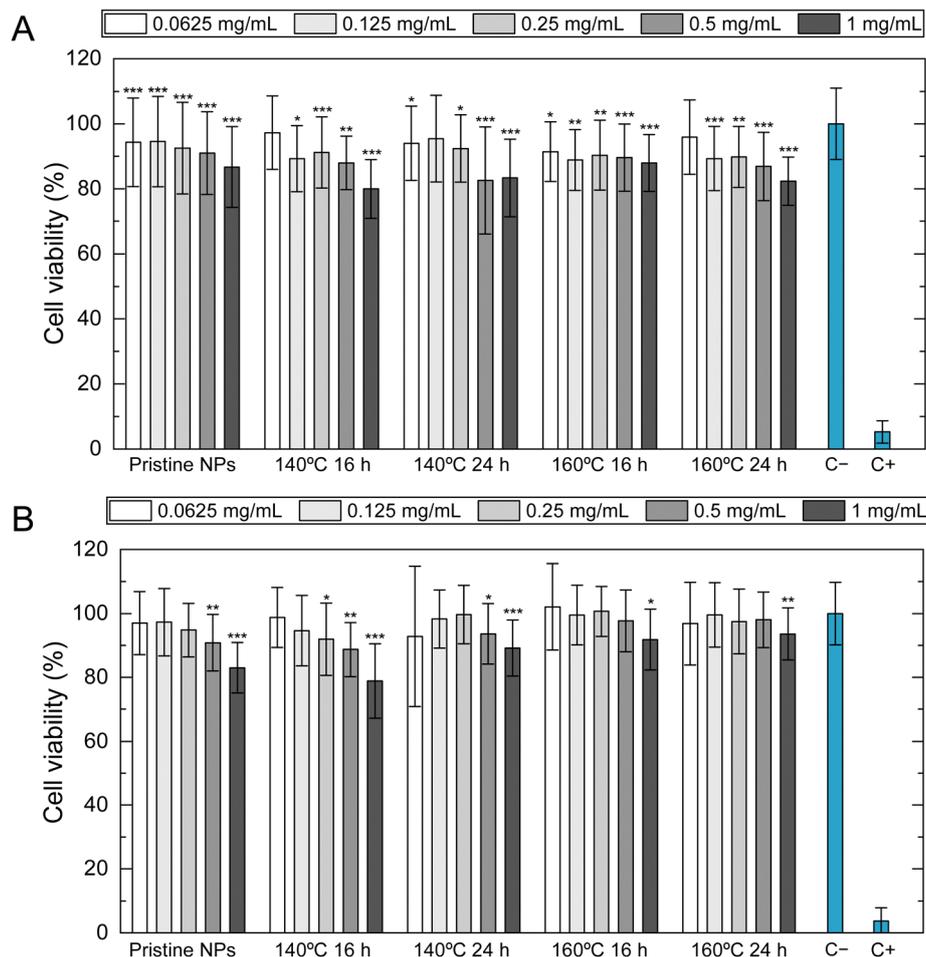
Fig. 7 *In vitro* cytotoxicity assays: cell viability (%) was measured by the direct method using resazurin after 24 hours of exposure to pristine NPs and SPIONs subjected to further hydrothermal treatment at different temperatures and durations. (A) HFFF2 cell line (representing a healthy cell line), (B) WM938b cell line (representing a tumorous cell line). Data are expressed as average ± standard deviation from at least three independent experiments. *$p < 0.05$, **$p < 0.005$, ***$p < 0.001$ compared to the negative control (C−).

WM938b cells. The control groups for each time point were not treated with SPIONs and, as expected, did not display any blue deposits. Fig. 8 shows images taken at 1 h, 6 h, and 24 h of cell exposure to NPs. The uptake of SPIONs by fibroblasts was found to increase with incubation time. However, HFFF2 cells exhibited relatively lower levels of internalization of pristine NPs, as evidenced by fewer intense blue deposits within the cells. The NPs tended to accumulate in higher quantities around the cellular membrane in melanoma cells. At the 24-hour mark, highly concentrated regions surrounded the cells, with less actual internalization, as the NPs primarily encircled the cells. Additionally, no discernible qualitative difference was observed in the internalization of pristine NPs compared to those that underwent hydrothermal treatment. It was impossible to differentiate the level of internalization among SPIONs subjected to different hydrothermal treatment conditions, as the images obtained appeared quite similar.

Various aspects related to the morphological characterization of NPs, including physical properties such as shape, size, and surface charge, can significantly impact their cellular uptake. The size of NPs, in particular, can profoundly affect the rate and pathway of cellular internalization.[61,62] In a study conducted by Chithrani *et al.*[63] on the cellular internalization of NPs of different sizes (14, 50, and 74 nm) in HeLa cells, the most efficient uptake was observed for 50 nm NPs, suggesting that there may be an optimal size for cell uptake. Similarly, HFFF2 cells showed a more significant uptake of larger SPIONs that underwent hydrothermal treatment (16.0 to 19.8 nm) compared to smaller, pristine NPs.

The shape of NPs can also greatly influence their uptake and interactions with cellular components. Several studies have been conducted to examine the effects of shape on cellular uptake. Quasi-spherical NPs provide fewer binding sites to the cell membrane due to their curved surface, resulting in less internalization. In contrast, NPs with sharp edges penetrate cell membranes more effectively, leading to greater internalization.[61,62] In an investigation by Nizamov *et al.*[64] on the drug delivery efficiency of iron oxide NPs, it was found that doxorubicin-loaded cubic NPs were more toxic to LNCaP and PC-3 cells than spherical ones. This suggests that the cubic
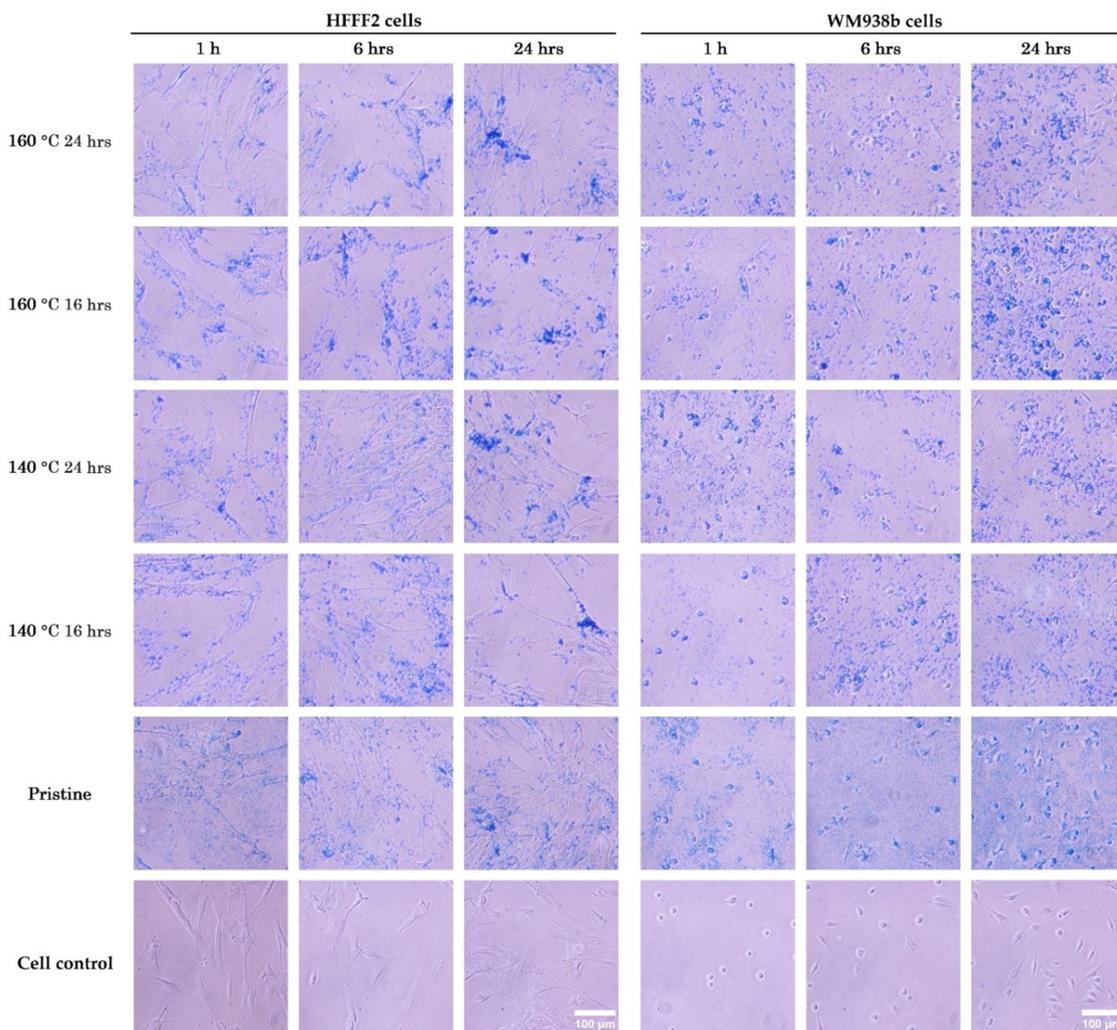
Fig. 8 Internalization studies using Prussian blue staining were conducted on HFFF2 (a healthy cell line) and WM938b cells (a tumorous cell line) after 1, 6, and 24 hours of exposure to 0.1 mg mL^{-1} of pristine NPs and SPIONs subjected to different hydrothermal treatment conditions.

shape of NPs could potentially enhance their cellular internalization and cytotoxicity.

3.4. Magnetic hyperthermia *in vitro*

To gain a deeper understanding of the magnetic behavior of SPIONs internalized by both normal and tumoral cells, magnetic hyperthermia measurements were conducted on HFFF2 and WM938b cell lines after 24 hours of exposure to NPs at a concentration of 5 mg mL^{-1}. The primary purpose of this experiment was to evaluate if SPIONs under these conditions could attain magnetic hyperthermia temperatures between 42 and 45 °C. An AMF was applied until the temperature reached 43.5 °C. The field was then turned off until the temperature cooled to 43 °C, then turned on again until the temperature rose to 44 °C. This alternating pulsed magnetic field was applied four times. Due to the intrinsic delay of the magnetic hyperthermia equipment, the magnetic field was turned off at 44 °C to prevent exceeding the upper limit of 45 °C. Fig. 9A and B shows the applied AMF as described and the registered

temperature for pristine NPs and 140 °C 16 h NPs when in contact with the HFFF2 cell line.

Pristine NPs could not reach the temperatures required for magnetic hyperthermia, as by the end of the 15-minute experiment, the temperature barely reached 40 °C. In contrast, all SPIONs subject to hydrothermal treatment reached 43.5 °C in approximately three and a half minutes. The period of the oscillations between 42 and 45 °C, observed during the pulses of the applied AMF, was approximately 50 seconds. These results are consistent with the previous findings on SAR and temperature increase values, revealing that pristine SPIONs cannot reach the minimum temperature rise necessary for magnetic hyperthermia under these experimental conditions. SPIONs subjected to hydrothermal treatment exhibit high responsiveness to magnetic field intensity, quickly reaching the required temperatures, indicating their potential utility as effective agents for magnetic hyperthermia. Fig. 10A and B shows that SPIONs in contact with melanoma cells reveal the same behavior regarding this magnetic hyperthermia analysis.
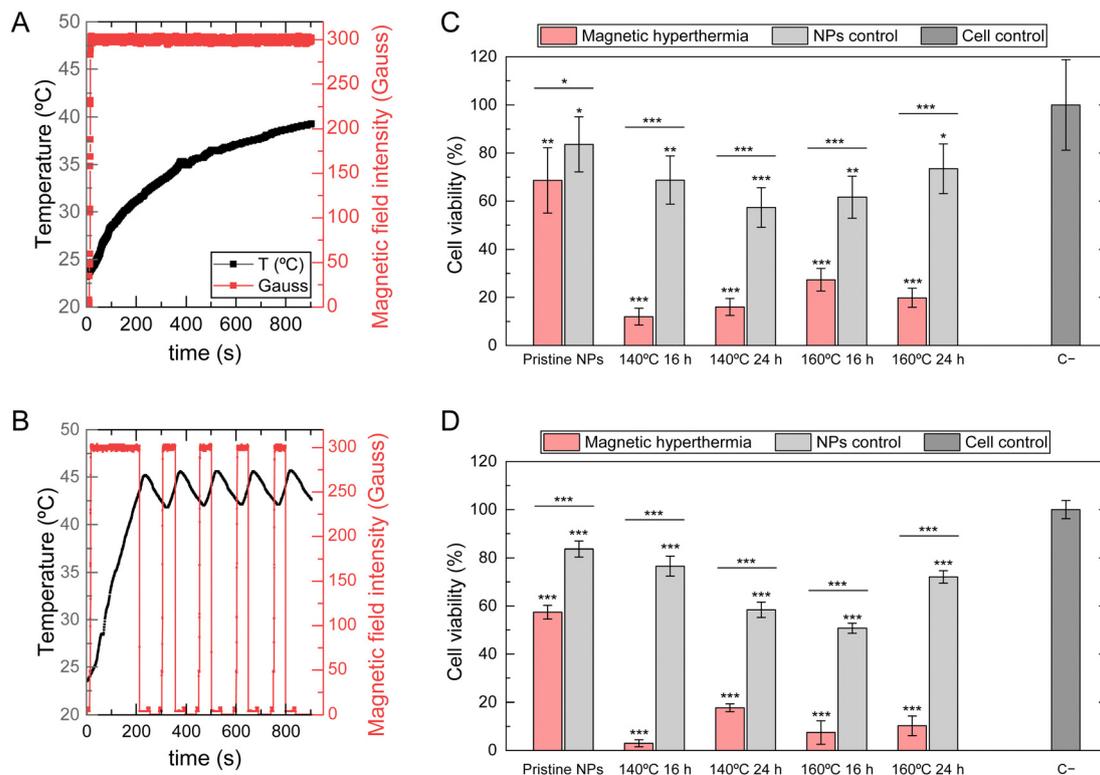
Fig. 9 Magnetic hyperthermia measurements were performed *in vitro* using the HFFF2 cell line (representing healthy cells): (A) heating curve (black) of pristine NPs at a concentration of 5 mg mL^{-1} obtained after 15 minutes of application of an alternating magnetic field (black) with an intensity of 24 kA m^{-1} and a frequency of 388.4 kHz. (B) Heating curve (black) of SPIONs treated at 140 °C for 16 h (representative of hydrothermal treatment) at a concentration of 5 mg mL^{-1} obtained after 15 minutes of "on and off" application of an alternating magnetic field (red) with an intensity of 24 kA m^{-1} and a frequency of 388.4 kHz, maintaining the temperature between 42 °C and 45 °C. (C) Cell viability measured using the resazurin assay immediately after applying the alternating magnetic field; (D) cell viability measured under the same conditions 24 hours later. Data are expressed as average ± standard deviation for at least three independent experiments. *$p < 0.05$, **$p < 0.005$, ***$p < 0.001$ compared to the negative control (C−) (symbol above column) or to NP control (symbol above horizontal line).

To evaluate the impact of magnetic hyperthermia on both normal (HFFF2) and melanoma (WM938b) cell lines, cell viability was assessed using a resazurin assay immediately after the application of the AMF and again 24 h later to further investigate the impact of magnetic hyperthermia on the cell cultures. A NP control was established for each nanoparticle type: a cell culture that was not exposed to the AMF but contained the same concentration of NPs (5 mg mL^{-1}) to distinguish between the cytotoxic effects of NPs and effects of magnetic hyperthermia. The results presented in Fig. 9C and D show the percentage of HFFF2 cell viability immediately after undergoing magnetic hyperthermia treatment and 24 hours later, respectively. These results demonstrate that, although the pristine NPs did not reach the desired magnetic hyperthermia range, the exposure to the AMF reduced cell viability 24 hours after its application. This effect may be related to the generation of hot spots in specific cellular locations, which cannot be measured by the equipment used as it measures the temperature in the medium.[16] Compared to samples that underwent hydrothermal treatment, a significant difference in cell viability was observed immediately and 24 hours after AMF application. Despite the reduction in cell viability caused by the high NPs

concentration, the application of AMF significantly reduced cell viability from 60–70% to approximately 10–20%.

Analyzing the effects of magnetic hyperthermia on melanoma cells (Fig. 10), it is evident that pristine NPs significantly decrease cell viability after applying an AMF, even though magnetic hyperthermia temperatures are not achieved. In this case, the presence of NPs alone is more significant, causing a considerable reduction in cell viability, even without applying an AMF. The experimental setup may also cause this reduction. The NPs control samples were subjected to the same protocol except for the hyperthermia part. Therefore, additional stress and the presence of NPs may have contributed to a higher decrease in cell viability. Additionally, this effect is more prolonged, with a continuous decrease in cell viability observed 24 hours after AMF application. These results suggest melanoma cells are more sensitive to the produced NPs, which could benefit cancer treatment.

4. Conclusions

The production of magnetic nanoparticles for biomedical applications should follow specific principles to enable their
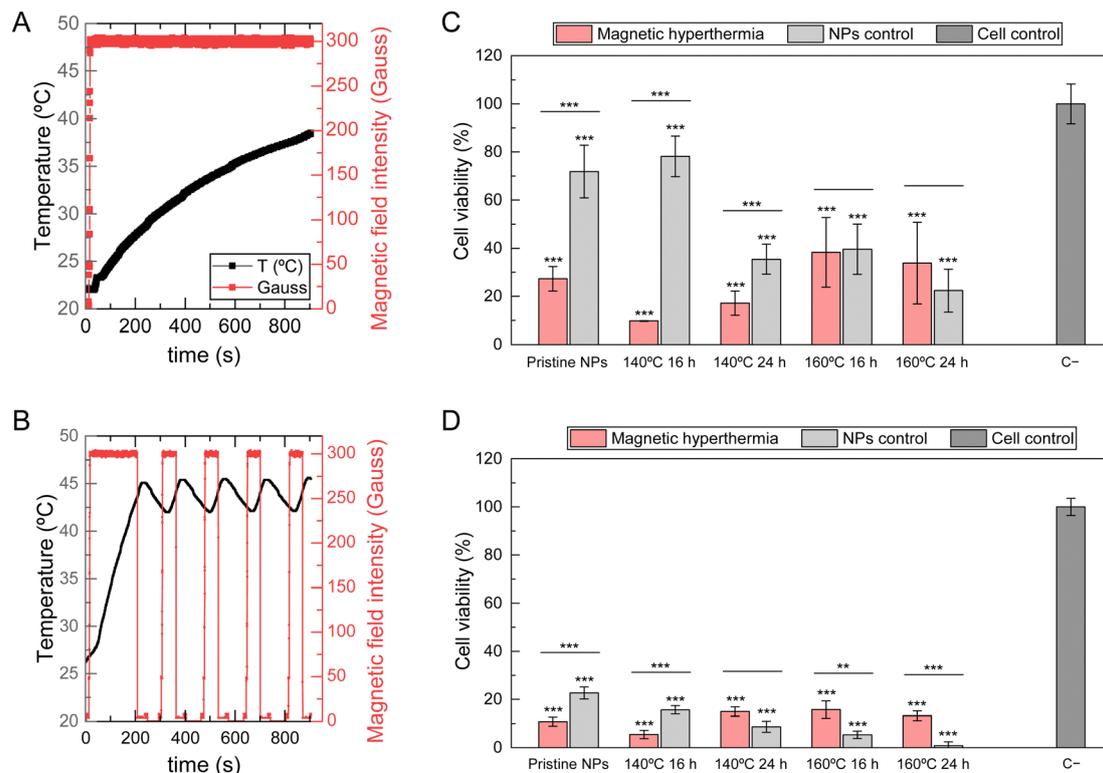
Fig. 10 Magnetic hyperthermia measurements were performed *in vitro* using the WM938b cell line (representing a tumor cells): (A) heating curve (black) of pristine NPs at a nanoparticle concentration of 5 mg mL^{-1} obtained after 15 minutes of application of an alternating magnetic field (black) with an intensity of 24 kA m^{-1} and a frequency of 388.4 kHz. (B) Heating curve (black) of SPIONs treated at 140 °C for 16 h (representative of hydrothermal treatment) at a nanoparticle concentration of 5 mg mL^{-1} obtained after 15 minutes of "on and off" application of an alternating magnetic field (red) with an intensity of 24 kA m^{-1} and a frequency of 388.4 kHz, maintaining the temperature between 42 °C and 45 °C. (C) Cell viability measured using resazurin immediately after applying the alternating magnetic field; (D) cell viability measured under the same conditions 24 hours after. Data are expressed as average ± standard deviation for at least three independent experiments. *$p < 0.05$, **$p < 0.005$, ***$p < 0.001$ compared to negative control (C−) (symbol above column) or compared to NP control (symbol above horizontal line).

actual use in medicine rather than being limited to laboratory studies. The synthesis method must be simple, reproducible, with high yield, and free of toxic solvents, among other requirements. Additionally, in the case of SPIONs, these should exhibit high crystallinity and high saturation magnetization while maintaining their magnetic properties over the intended usage period. In this work SPIONs were produced by combining chemical co-precipitation technique with hydrothermal treatment. The NPs size increased from 9 to 20 nm, with a morphological change from spherical to cubic/rectangular shapes. These changes led to an improvement in magnetic saturation from 58 to 73 emu g^{-1} at RT. After hydrothermal treatment, the SPIONs remained stable in water during storage and retained their magnetic properties under physiological conditions (body temperature), specifically their superparamagnetic properties. Magnetic hyperthermia measurements assessed their potential for cancer treatment in normal and melanoma cell lines. A significant decrease in cell viability was observed when cells were exposed to NPs after hydrothermal treatment, with a more pronounced effect in melanoma cells. These results demonstrate the high potential of this synthesis method for producing SPIONs for cancer treatment *via* magnetic hyperthermia.

Data availability

The data supporting this article have been included in the manuscript. Any additional detail may be requested to the authors.

Conflicts of interest

The authors declare that they have no known competing financial interests that could have appeared to influence the work reported in this paper.

Acknowledgements

References

1 P. I. P. Soares, J. Romão, R. Matos, J. C. Silva and J. P. Borges, *Prog. Mater. Sci.*, 2021, **116**, 100742.

2 C. I. P. Chaparro, L. R. Loureiro, M. A. Valente, P. A. Videira, J. P. Borges and P. Soares, Application of Hyperthermia for Cancer Treatment: Synthesis and Characterization of Magnetic Nanoparticles and their internalization on Tumor Cell Lines, IEEE 6th Portuguese Meeting on Bioengineering (ENBENG), Lisbon, Portugal, 2019, pp. 1–4.

3 P. I. Soares, I. M. Ferreira, R. A. Igreja, C. M. Novo and J. P. Borges, *Recent Pat. Anticancer Drug Discovery*, 2012, **7**, 64–73.

4 P. I. Soares, F. Lochte, C. Echeverria, L. C. Pereira, J. T. Coutinho, I. M. Ferreira, C. M. Novo and J. P. Borges, *Nanotechnology*, 2015, **26**, 425704.

5 P. I. Soares, D. Machado, C. Laia, L. C. Pereira, J. T. Coutinho, I. M. Ferreira, C. M. Novo and J. P. Borges, *Carbohydr. Polym.*, 2016, **149**, 382–390.

6 P. I. P. Soares, C. A. T. Laia, A. Carvalho, L. C. J. Pereira, J. T. Coutinho, I. M. M. Ferreira, C. M. M. Novo and J. P. Borges, *Appl. Surf. Sci.*, 2016, **383**, 240–247.

7 F. J. T. M. Tavares, P. I. P. Soares, J. C. Silva and J. P. Borges, *Int. J. Mol. Sci.*, 2023, **24**, 1128.

8 A. Carvalho, M. C. Goncalves, M. B. Martins, D. Meixedo and G. Feio, *Magn. Reson. Imaging*, 2013, **31**, 610–612.

9 T. Hoare, J. Santamaria, G. F. Goya, S. Irusta, D. Lin, S. Lau, R. Padera, R. Langer and D. S. Kohane, *Nano Lett.*, 2009, **9**, 3651–3657.

10 A. Gonçalves, F. V. Almeida, J. P. Borges and P. I. P. Soares, *Gels*, 2021, **7**, 28.

11 A. Gonçalves, B. T. Simões, F. V. Almeida, S. N. Fernandes, M. Valente, T. Vieira, C. Henriques, J. P. Borges and P. I. P. Soares, *Biomater. Adv.*, 2023, **145**, 213275.

12 C. I. P. Chaparro, B. T. Simoes, J. P. Borges, M. Castanho, P. I. P. Soares and V. Neves, *Pharmaceutics*, 2023, **15**, 2316.

13 P. I. P. Soares and J. P. Borges, *Prog. Nat. Sci.:Mater. Int.*, 2021, **31**, 835–844.

14 I. Obaidat, B. Issa and Y. Haik, *Nanomaterials*, 2015, **5**, 63–89.

15 H. Etemadi and P. G. Plieger, *Adv. Ther.*, 2020, **3**, 2000061.

16 C. Pucci, A. Degl'Innocenti, M. Belenli Gümüş and G. Ciofani, *Biomater. Sci.*, 2022, **10**, 2103–2121.

17 R. Massart, *US Pat.*, US4329241A, 1980.

18 H. Gavilán, S. K. Avugadda, T. Fernández-Cabada, N. Soni, M. Cassani, B. T. Mai, R. Chantrell and T. Pellegrino, *Chem. Soc. Rev.*, 2021, **50**, 11614–11667.

19 R. Hergt and S. Dutz, *J. Magn. Magn. Mater.*, 2007, **311**, 187–192.

20 D. Bonvin, D. T. L. Alexander, A. Millan, R. Pinol, B. Sanz, G. F. Goya, A. Martinez, J. A. M. Bastiaansen, M. Stuber, K. J. Schenk, H. Hofmann and M. Mionic Ebersold, *Nanomaterials*, 2017, **7**, 225.

21 Q. Li, C. W. Kartikowati, S. Horie, T. Ogi, T. Iwaki and K. Okuyama, *Sci. Rep.*, 2017, **7**, 9894.

22 A. H. Lu, E. L. Salabas and F. Schuth, *Angew. Chem., Int. Ed.*, 2007, **46**, 1222–1244.

23 W. Wu, Q. He and C. Jiang, *Nanoscale Res. Lett.*, 2008, **3**, 397–415.

24 J. Li, X. Shi and M. Shen, *Part. Part. Syst. Charact.*, 2014, **31**, 1223–1237.

25 M. Daschner de Tercero, C. Röder, U. Fehrenbacher, U. Teipel and M. Türk, *J. Nanopart. Res.*, 2014, **16**, 1–27.

26 D. Bonvin, H. Hofmann and M. Mionic Ebersold, *J. Nanopart. Res.*, 2016, **18**, 376.

27 F. Ozel and H. Kockar, *J. Magn. Magn. Mater.*, 2015, **373**, 213–216.

28 N. Torres-Gómez, O. Nava, L. Argueta-Figueroa, R. García-Contreras, A. Baeza-Barrera and A. R. Vilchis-Nestor, *J. Nanomater.*, 2019, **2019**, 7921273.

29 P. I. Soares, A. M. Alves, L. C. Pereira, J. T. Coutinho, I. M. Ferreira, C. M. Novo and J. P. Borges, *J. Colloid Interface Sci.*, 2014, **419**, 46–51.

30 M. Talelli, C. J. Rijcken, T. Lammers, P. R. Seevinck, G. Storm, C. F. van Nostrum and W. E. Hennink, *Langmuir*, 2009, **25**, 2060–2067.

31 R. J. R. Matos, C. I. P. Chaparro, J. C. Silva, M. A. Valente, J. P. Borges and P. I. P. Soares, *Carbohydr. Polym.*, 2018, **198**, 9–16.

32 Z. P. Aguilar, in *Nanomaterials for Medical Applications*, ed. Z. P. Aguilar, Elsevier, 2013, pp. 293–360, DOI: 10.1016/B978-0-12-385089-8.00007-8.

33 A. Khorsand Zak, W. H. A. Majid, M. E. Abrishami and R. Yousefi, *Solid State Sci.*, 2011, **13**, 251–256.

34 A. Cervellino, R. Frison, G. Cernuto, A. Guagliardi and N. Masciocchi, *J. Appl. Crystallogr.*, 2014, **47**, 1755–1761.

35 S. Ge, X. Shi, K. Sun, C. Li, C. Uher, J. R. Baker, Jr., M. M. Banaszak Holl and B. G. Orr, *J. Phys. Chem. C*, 2009, **113**, 13593–13599.

36 V. D. Mote, Y. Purushotham and B. N. Dole, *J. Theor. Appl. Phys.*, 2012, **6**, 6.

37 P. W. Dunne, A. S. Munn, C. L. Starkey, T. A. Huddle and E. H. Lester, *Philos. Trans. R. Soc., A*, 2015, **373**, 20150015.

38 A. Chatzigoulas, K. Karathanou, D. Dellis and Z. Cournia, *J. Chem. Inf. Model.*, 2018, **58**, 2380–2386.

39 T. K. Sau and A. L. Rogach, *Adv. Mater.*, 2010, **22**, 1781–1804.

40 P. M. Carvalho, M. R. Felicio, N. C. Santos, S. Goncalves and M. M. Domingues, *Front. Chem.*, 2018, **6**, 237.

41 L. Xu, X. Wang, Y. Liu, G. Yang, R. J. Falconer and C.-X. Zhao, *Adv. NanoBiomed Res.*, 2022, **2**, 2100109.

42 M. Fan, Y. Ma, H. Tan, Y. Jia, S. Zou, S. Guo, M. Zhao, H. Huang, Z. Ling, Y. Chen and X. Hu, *Mater. Sci. Eng., C*, 2017, **71**, 67–74.

43 A. V. Samrot, C. S. Sahithya, J. Selvarani A, S. K. Purayil and P. Ponnaiah, *Curr. Res. Green Sustainable Chem.*, 2021, **4**, 100042.

44 S. Bhattacharjee, *J. Controlled Release*, 2016, **235**, 337–351.

45 K. Hidehiro and I. Motoyuki, *Sci. Technol. Adv. Mater.*, 2010, **11**, 044304.

46 J. Faraudo, J. S. Andreu and J. Camacho, *Soft Matter*, 2013, **9**, 6654.

47 A. Ercuta and M. Chirita, *J. Cryst. Grow.*, 2013, **380**, 182–186.

48 L. S. Darken and R. W. Gurry, *J. Am. Chem. Soc.*, 1946, **68**, 798–816.

49 E. N. Lysenko, A. P. Surzhikov, S. P. Zhuravkov, V. A. Vlasov, A. V. Pustovalov and N. A. Yavorovsky, *J. Therm. Anal. Calorim.*, 2014, **115**, 1447–1452.

50 T. J. Daou, G. Pourroy, S. Bégin-Colin, J. M. Grenèche, C. Ulhaq-Bouillet, P. Legaré, P. Bernhardt, C. Leuvrey and G. Rogez, *Chem. Mater.*, 2006, **18**, 4399–4404.

51 G. Joaquín and S. Gloria, *J. Phys.: Condens. Matter*, 2004, **16**, R145.

52 W. Friedrich, *J. Phys.: Condens. Matter*, 2002, **14**, R285.

53 R. Aragón, J. P. Shepherd, J. W. Koenitzer, D. J. Buttrey, R. J. Rasmussen and J. M. Honig, *J. Appl. Phys.*, 1985, **57**, 3221–3222.

54 G. F. Goya, T. S. Berquó, F. C. Fonseca and M. P. Morales, *J. Appl. Phys.*, 2003, **94**, 3520–3528.

55 R. Prozorov, T. Prozorov, S. K. Mallapragada, B. Narasimhan, T. J. Williams and D. A. Bazylinski, *Phys. Rev. B:Condens. Matter Mater. Phys.*, 2007, **76**, 054406.

56 A. LeBrun and L. Zhu, *Theory and Applications of Heat Transfer in Humans*, 2018, pp. 631–667, DOI: **10.1002/9781119127420.ch29**.

57 X. Liu, M. D. Kaminski, Y. Guan, H. Chen, H. Liu and A. J. Rosengart, *J. Magn. Magn. Mater.*, 2006, **306**, 248–253.

58 S. Dutz and R. Hergt, *Int. J. Hyperthermia*, 2013, **29**, 790–800.

59 S. V. Jadhav, S.-H. Lee, D. S. Nikam, R. A. Bohara, S. H. Pawar and Y.-S. Yu, *New J. Chem.*, 2017, **41**, 1598–1608.

60 L. M. Cursaru, R. M. Piticescu, D. V. Dragut, R. Morel, C. Thébault, M. Carrière, H. Joisten and B. Dieny, *Nanomaterials*, 2020, **10**, 1500.

61 R. Augustine, A. Hasan, R. Primavera, R. J. Wilson, A. S. Thakor and B. D. Kevadiya, *Mater. Today Commun.*, 2020, **25**, 101692.

62 A. Verma and F. Stellacci, *Small*, 2010, **6**, 12–21.

63 B. D. Chithrani, A. A. Ghazani and W. C. Chan, *Nano Lett.*, 2006, **6**, 662–668.

64 T. R. Nizamov, A. S. Garanina, I. S. Grebennikov, O. A. Zhironkina, O. S. Strelkova, I. B. Alieva, I. I. Kireev, M. A. Abakumov, A. G. Savchenko and A. G. Majouga, *Bionanoscience*, 2018, **8**, 394–406.